RSC Advances

ROYAL SOCIETY OF CHEMISTRY

PAPER

View Article Online
View Journal | View Issue

Check for updates

Cite this: *RSC Adv.*, 2023, **13**, 9377

Synthesis and upconversion emission studies of CaYF$_5$:Ho^{3+}/Yb^{3+} phosphor and its applications in optical thermometry, fingerprint detection, and security ink†

Kumar Shwetabh, Madan M. Upadhyay and K. Kumar *

Received 30th January 2023
Accepted 5th March 2023

DOI: 10.1039/d3ra00644a

rsc.li/rsc-advances

In this work, a CaYF$_5$:Ho^{3+}/Yb^{3+} upconversion phosphor was synthesized and its structural, morphological, and optical properties were studied. The upconversion emission study was performed at an excitation pump power density of 5 W cm^{-2} and emissions at 544 nm, 650 nm and 747 nm due to the $^5F_4(^5S_2) \rightarrow {}^5I_8$, $^5F_5 \rightarrow {}^5I_8$ and $^5F_4(^5S_2) \rightarrow {}^5I_7$ transitions of the Ho^{3+} ion, respectively were observed. From temperature-dependent upconversion spectra temperature sensitivity was calculated and sensitivity is found to be 14×10^{-3} K^{-1} for the synthesized upconversion phosphor. The photothermal conversion efficiency of the prepared sample in ethanol medium was tested. Moreover, the sample was used to develop latent fingerprints on various surfaces and good contrast in recorded images is observed. The invisible ink was prepared using the upconversion phosphor and then written words were recorded in upconversion emission mode.

1. Introduction

Inorganic materials doped with lanthanide ions have found tremendous applications across various fields like temperature sensing, bio-imaging, solar cells and security.[1–10] They have some unique features of converting NIR photons to intense visible or UV photons, atomic emissions like narrow line width and long lifetime. They are usually composed of a low phonon host matrix with suitable rare earth ions doped within it. The low phonon host matrix suppresses the non-radiative rates and promotes the photon emission efficiency of the upconversion phosphor. To date various materials have been synthesized to find the most suitable host material. AREF$_4$ is a class of materials that exhibit good emission intensity because these fluoride-based hosts possess very low phonon energy and they give specific lattice sites to dopant ions.[11–16] Both the chemical as well as physical properties affect the upconversion efficiency of a material hence engineering these conditions could lead to good results. Variation in experimental conditions could lead to changes in morphology, size, phase, stability, ion distribution, and surface defects. All these parameters can alter the energy transfer pathways which eventually help in the manipulation of upconversion efficiency. Sometimes this manipulation leads to the quenching of upconversion emission intensity. Due to this, it is a very difficult task to select a particular material that can show intense upconversion emission at low dopant ion concentration.

Gao *et al.* have prepared Ho^{3+}–Yb^{3+} co-doped hexagonal NaYF$_4$ nanoparticles which initially showed intense green emission compared to the red band but doping of Ce^{3+} leads to intense red emission.[11] It was concluded that non-radiative relaxation takes place between the energy states of Ho^{3+} to Ce^{3+} and which reduces green emission. Thus by variation in doping, we can alter luminescence according to our requirements. Commonly used upconversion materials are doped with Yb^{3+} ion since most of the upconversion materials use excitation in NIR spectral region. Yb^{3+} ion has two suitable energy levels $^2F_{5/2}$ and $^2F_{7/2}$ whose energy gap is around 10 000 cm^{-1} due to which Yb^{3+} ion shows absorption around the wavelength of 980 nm when doped into the host material. Although some other rare earth ions have similar energy gaps they are unable to absorb energy efficiently like Yb^{3+} ions due to a lack of large absorption cross-section around this energy value. The most efficient pair of rare earth ions for converting NIR to visible or UV are Er^{3+}–Yb^{3+}, Ho^{3+}–Yb^{3+} and Tm^{3+}–Yb^{3+} because sensitization through the Yb^{3+} ion enhances upconversion efficiency multiple times. The Ho^{3+}–Yb^{3+} pair is also used to achieve intense green emission.[17,18] Contrary to the Er^{3+} ion emission the Ho^{3+} ion gives only one emission in visible region and hence green colour purity of Ho^{3+} is found better than the Er^{3+} ion. Another benefit of using Ho^{3+}–Yb^{3+} pair over Er^{3+}/Yb^{3+} and Tm^{3+}/Yb^{3+} pairs is that latter pairs contain thermally coupled levels which limit its applicability when used for optical thermometric application but due to the absence of thermally coupled levels in Ho^{3+} ions, the doping of Ho^{3+} ions provide

---

Department of Physics, Optical Materials and Bio-imaging Research Laboratory, Indian Institute of Technology (Indian School of Mines), Dhanbad-826004, India. E-mail: kkumar@iitism.ac.in

† Electronic supplementary information (ESI) available. See DOI: https://doi.org/10.1039/d3ra00644a

relatively much better sensitivity using non-thermally coupled level method. The energy gap of 200 cm^{-1} to 2000 cm^{-1} limits the application of Er^{3+}/Yb^{3+} and Tm^{3+}/Yb^{3+} pairs for temperature sensing but the use of Ho^{3+}–Yb^{3+} pair can overcome this issue. Recently, Du *et al.* have synthesized Ho^{3+}/Yb^{3+} doped into $BaCaTiO_3$ ceramics and achieved intense upconversion emissions around 546 nm and 656 nm which they later used to calculate thermal sensitivity.[19] Tian *et al.* have shown that doping of Ho^{3+}/Yb^{3+} into $Y_2Ti_2O_7$ nanowires achieves bright upconversion emissions around 545 nm and 656 nm upon excitation with 980 nm radiation.[20] These works present Ho^{3+}/Yb^{3+} pairs as a potential candidate for visible upconversion emission.

In this work, authors have synthesized Ho^{3+}/Yb^{3+} doped $CaYF_5$ upconversion phosphor for the first time. $CaYF_5$ crystal belongs to a class of nonstoichiometric compounds $A_{1-x}R_xF_{2+x}$ crystal which is a product of the AF_2–RF_3 binary system.[4] This system produces various nonstoichiometric fluoride phases of the CaF_2–YF_3 system. These kind of crystals have come into the light for their extraordinary fluorescence properties when doped with rare earth ions. Due to low lattice phonon energy, these materials can show good upconversion luminescence along with high thermal and chemical stability. Recently Grzyb *et al.* have investigated the luminescence properties of rare-earth-doped $BaREF_5$ nanoparticles.[4] Luo *et al.* have synthesized Bi^{3+} doped $BaYF_5{:}Yb^{3+}/Er^{3+}$ upconversion nanoparticles with varying concentrations of Bi^{3+} ion and achieved enhanced luminescence intensity.[21] These reports indicate the potentiality of such materials for upconversion-based applications. However, due to phase-related difficulties, these materials are difficult to synthesize and hence haven't been explored much the spectroscopic properties and there is a need to investigate on luminescence properties of these materials. Also, there is no published report which could show the spectroscopic property of rare earth doped $CaYF_5$ particles. In this work, authors have successfully synthesized Ho^{3+}/Yb^{3+} co-doped $CaYF_5$ crystals and then investigated its upconversion luminescence properties. Further, the synthesized nanoparticles were demonstrated for fingerprint detection and security ink applications.

2. Experimental section

2.1. Materials

For this work, precursors used are yttrium oxide (Y_2O_3), ytterbium oxide (Yb_2O_3), and holmium oxide (Ho_2O_3) (Sigma-Aldrich, 99.99%). Calcium carbonate ($CaCO_3$), ammonium fluoride (NH_4F), oleic acid ($C_{17}H_{33}COOH$), 1-octadecane ($C_{18}H_{36}$), and hydrochloric acid (HCl) were purchased from Alpha Aesar. All the chemicals were used as received without further purification.

2.2. Synthesis of upconversion phosphor

In this synthesis, the rare earth chlorides $RECl_3$ (RE = Y, Yb, Ho) were used as precursors for the sample. The concentrations of Y^{3+}, Yb^{3+}, and Ho^{3+} were set to 89.5, 10 and 0.5 mol%, respectively for the optimized sample. For this optimized sample, 451.1 mg of Y_2O_3, 44 mg of Yb_2O_3, 2.1 mg of Ho_2O_3, and 150 mg of $CaCO_3$ were dissolved in hydrochloric acid separately by heating, and after getting a transparent solution the excess of HCl was removed by evaporating. Further, 10 ml of oleic acid and 10 ml of 1-octadecane was mixed into a 100 ml three-neck round bottom flask at 150 °C under a Nitrogen environment. This mixing leads to a transparent solution which was left for cooling to room temperature. The as-prepared rare earth chloride powders were poured into this cooled transparent solution and then stirred for 30 minutes at 60 °C to form the metal-oleate complex. Then, as prepared calcium chloride powder was added to this metal-oleate solution, and this mixture was stirred continuously in a nitrogen environment for 30 minutes. The 186 mg NH_4F was dissolved in 5 ml methanol and a solution was obtained. This solution was then mixed with main solution with stirring. Now the temperature of vessel was raised slowly to 300 °C and maintained at this temperature for 60 minutes. After completing the reaction heating was turned off and the solution was cooled down to room temperature. After arriving at room temperature excess ethanol was added to the solution to get precipitate. The precipitate was rinsed several times with ethanol and hexane (volume ratio 1 : 1) and then dried overnight at 60 °C. Finally, the dried powder was crushed and kept for further use.

2.3. Material characterization

Structural and phase properties of synthesized upconversion phosphor were investigated using Rigaku Smartlab high-resolution X-ray diffractometer (HR-XRD). Analysis of the surface morphology of upconversion phosphor particles was performed on Supra 55 (Carl Zeiss, Germany) Scanning electron microscopy (SEM) and Energy-dispersive X-ray Spectroscopy (EDX). Near infrared-ultraviolet-visible (NIR-UV-Vis) spectroscopy was performed on Agilent Cary 500 attached with integrating sphere. Fourier transform infrared spectroscopy (FTIR) was performed using PerkinElmer Spectrum 2.0 spectroscope which shows the presence of different functional groups in the as-synthesized upconversion phosphor. Upconversion emission spectra were recorded on Avantes ULS2048X58 charge-coupled device (CCD) equipped with a 980 nm diode laser and optical fiber. The temperature-dependent upconversion spectra were recorded using the same diode laser, CCD, and optical fiber integrated with the home made small heater and thermocouple. The temperature of heater was controlled using a potentiometer during the measurement. Photothermal conversion measurement was also made on above system. The thermocouple was inserted into a cuvette and then the temperature change was measured. Decay curves of Ho^{3+} green emission were measured using 980 nm diode laser, mechanical chopper, monochromator, and a fast silicon photodetector. For recording of decay curves a digital oscilloscope (200 GHz) was used.

3. Results and discussions

3.1. X-ray diffraction study

XRD pattern of as-synthesized upconversion phosphor was obtained and analysed. The XRD pattern reveals the cubic phase of

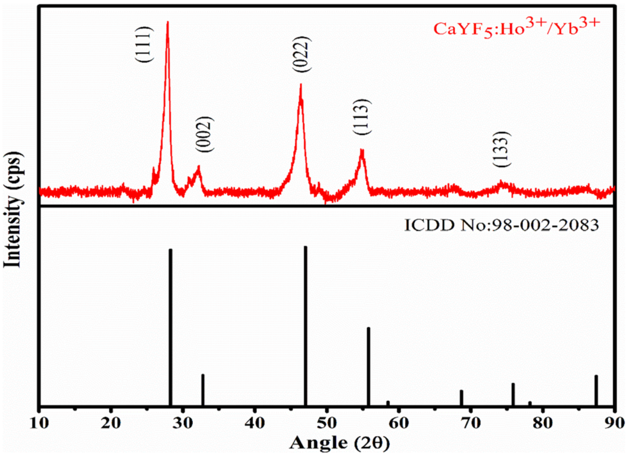

Fig. 1 XRD pattern of as-synthesized $CaYF_5:Ho^{3+}/Yb^{3+}$ upconversion phosphor with reference pattern.

the synthesized $CaYF_5$ crystal. Recorded XRD pattern with corresponding reference pattern is shown in Fig. 1. Diffraction peaks are well matched with the reference phase. The diffraction peaks are little shifted toward lower 2θ value which can be attributed to the incorporation of a bigger Yb^{3+} ion into the $CaYF_5$ lattice.

3.2. Scanning electron microscopy study

The surface morphology and size information of the synthesized $CaYF_5:Ho^{3+}/Yb^{3+}$ nanoparticles was obtained using a scanning electron microscope (SEM) image. The as-obtained SEM image in Fig. 2(a) shows the particles looks like spherical shape but agglomerated with other. Inset of the Fig. 2(a) shows size distribution for small spherical shape like particles and mean size is found around 32 nm. However, it is a rough estimate as recorded image has large field of view compared to the size of the particles. Further resolution in SEM image was not possible due to charging the particles. The EDX spectrum in Fig. 2(b) shows the presence of all elements *viz.* Ca, Y, F, Ho, and Yb in the synthesized sample. However there is a slight difference in the calculated and observed weight% due to presence of oleic acid coating on surface.

3.3. UV-Vis-NIR spectroscopy

UV-Vis-NIR spectroscopy was performed in diffuse reflectance spectroscopy (DRS) mode in 200 nm to 1200 nm range using a spectrophotometer equipped with UV, visible, and NIR light sources. In DRS mode, the ratio of reflected light to the incident light from the surface of the sample is measured as a function of wavelength. Recorded spectrum (Fig. 3) shows an absorption band around 980 nm which is the prominent absorption band due to Yb^{3+} ions while the absorption peaks around 642 nm, 534 nm, and 448 nm are due to the Ho^{3+} ions. The absorption band of Yb^{3+} ion around 980 nm is due to the transition from $^2F_{7/2}$ to $^2F_{5/2}$ level while the absorption peaks of Ho^{3+} ion around 642 nm, 534 nm, and 448 nm are due to the transition from ground level $^5I_8$ to excited levels $^5F_5$, $^5S_2$ and $^3K_8$, respectively.[22] With the help of DRS, the band gap was calculated using the Kubelka–Munk relation which relates the absorption and scattering coefficient with diffuse reflectance, and the Tauc relation which relates the band gap to linear absorption coefficients. According to Kubelka–Munk relation

$$\frac{K}{S} = \frac{(1-R)^2}{2R} \tag{i}$$

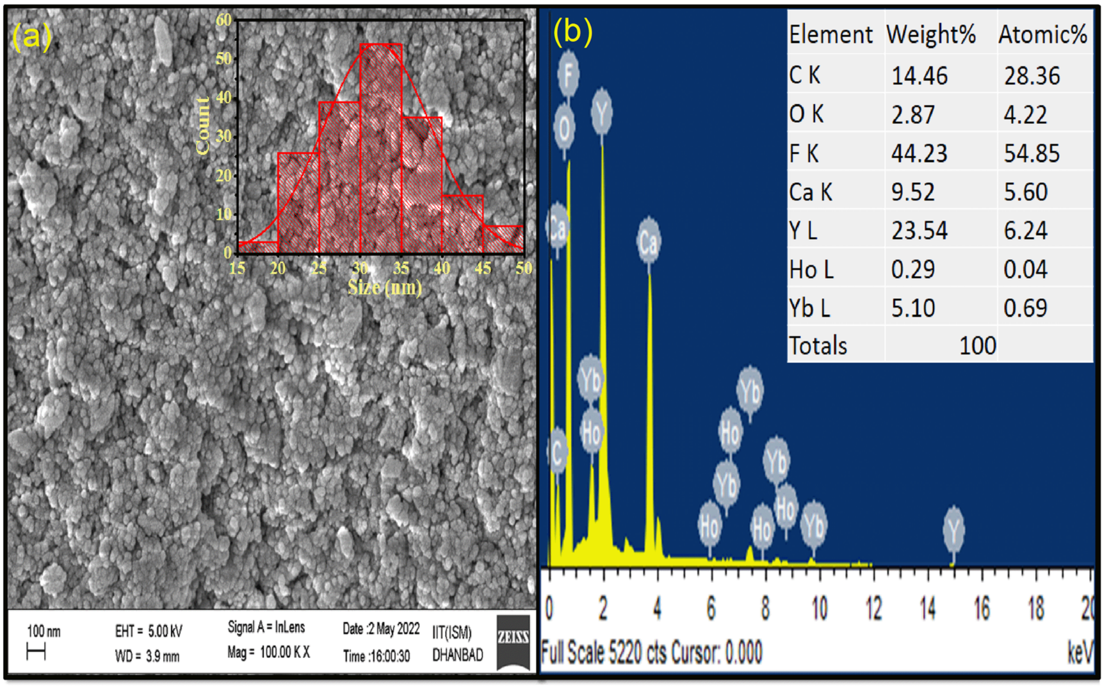

Element	Weight%	Atomic%
C K	14.46	28.36
O K	2.87	4.22
F K	44.23	54.85
Ca K	9.52	5.60
Y L	23.54	6.24
Ho L	0.29	0.04
Yb L	5.10	0.69
Totals	100	

Fig. 2 (a) FESEM image (inset: size distribution) and (b) EDX spectrum of as-synthesized $CaYF_5:Ho^{3+}/Yb^{3+}$ upconversion phosphor.

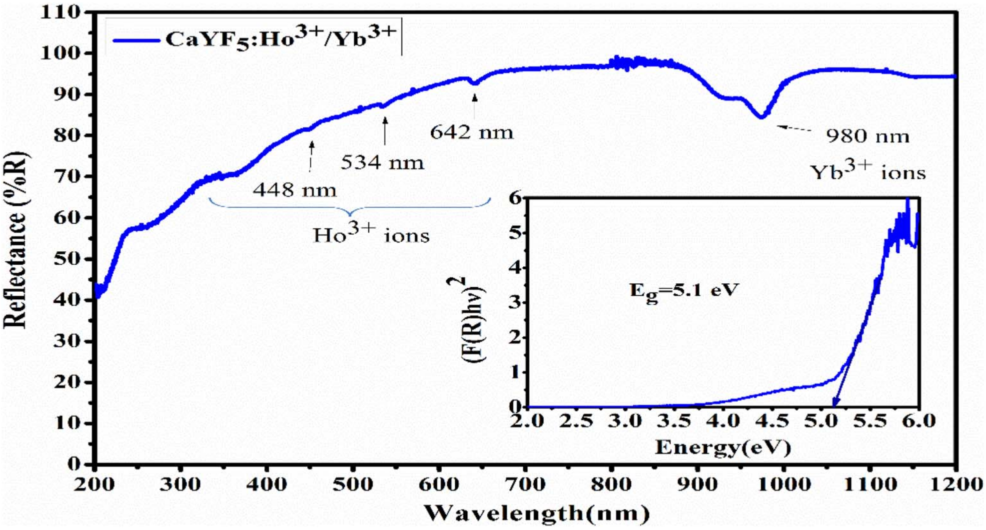

Fig. 3 UV-Vis-NIR spectrum of synthesized $CaYF_5:Ho^{3+}/Yb^{3+}$ upconversion phosphor (inset: band gap calculation using Tauc plot).

Here

$$\frac{K}{S} = F(R) \tag{ii}$$

$F(R)$ is called as Kubelka–Munk function and R is the reflectance of the sample compared to the reference.[23,24] In our case reference is $BaSO_4$ powder.

Tauc relation is given by

$$\alpha h\nu = C(h\nu - E_g)^n \tag{iii}$$

where, α, C, and $h\nu$ are the absorption coefficient, proportionality constant, and energy of incident photon respectively. For perfectly diffuse reflection the value of the absorption coefficient (K) takes the value of 2α.[25] Here we also assume the scattering coefficient is constant during a change in wavelength. The $CaYF_5$ lattice shows direct allowed transition hence value of n will be 1/2 in this case.[7,26] This value can be found by fitting the Tauc plot for all four n values corresponding to each type of band gap transition. Combinations of the above three equations yield an equation

$$[F(R)h\nu]^2 = C(h\nu - E_g) \tag{iv}$$

Now using this eqn (iv) we plot a graph between $[F(R)h\nu]^2$ and $h\nu$ and then extrapolate the linear part of this curve to zero this gives the value of the band gap. Band gap of 5.1 eV was found for the synthesized upconversion phosphor. Inset of Fig. 3 shows plot for band gap calculation.

3.4. Fourier transformed infrared spectroscopy

Fourier-transformed infrared spectroscopy (FTIR) was performed within the energy range 400–4000 cm^{-1} to identify the organic moieties present in the synthesized sample. Presence of

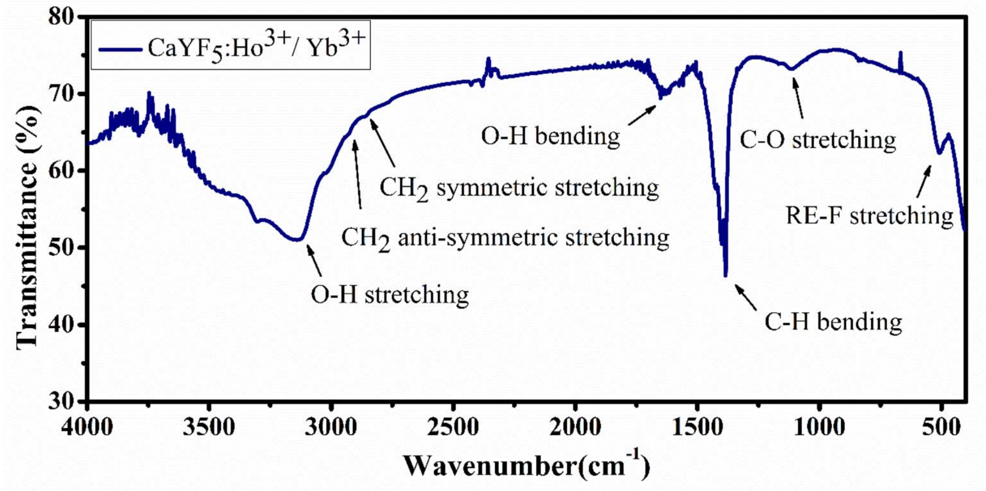

Fig. 4 FTIR spectrum of synthesized $CaYF_5:Ho^{3+}/Yb^{3+}$ sample.

oleic acid and some water content is observed in the sample based on the positions of the absorption bands. Each absorption peak is assigned and shown in Fig. 4.

3.5. Upconversion spectroscopy studies

Upconversion spectra for prepared $CaYF_5$:Ho^{3+}/Yb^{3+} upconversion phosphors were recorded using 980 nm diode laser. Sample was optimized for the maximum upconversion emission by varying Ho^{3+} ion concentration from 0.1 mol% to 1.0 mol% and keeping Yb^{3+} fixed at 10.0 mol%. After getting maximum emission at particular Ho^{3+} concentration, this concentration was fixed and then Yb^{3+} ion concentration was varied from 1.0 mol% to 20 mol%. The variation of upconversion emission against Ho^{3+} and Yb^{3+} concentrations is shown in ESI Fig. S1.† The optimum upconversion is observed for Ho^{3+} and Yb^{3+} concentrations of 0.5 mol% and 10 mol%, respectively. Further studies are done for this optimized sample only. The emission spectrum of optimized sample is shown in Fig. 5. The most intense emission is observed at 544 nm with weak emissions at 650 nm and 747 nm wavelength. The band assignment for each peak is given in Fig. 5(a).

The Yb^{3+} ion absorbs a 980 nm wavelength photon and makes a transition from $^2F_{7/2}$ to $^2F_{5/2}$ level. Apart from Yb^{3+} ion absorption, Ho^{3+} also absorbs some of the 980 nm photons and makes the transition from ground state $^5I_8$ to excited state $^5I_6$ which is referred to as ground state absorption (GSA). After reaching the $^5I_6$ state absorption of one more photon by the Ho^{3+} ion leads to excited state absorption (ESA) which makes this activator ion get through the level to $^5F_4(^5S_2)$. Now the absorbed energy by the Yb^{3+} ion is transferred to the Ho^{3+} ion by various energy transfer (ET) processes indicated in the energy level diagram. Energy transfer processes are labelled as ET_1 and ET_2 which refers to the transfer of energy from excited state $^2F_{5/2}$ of Yb^{3+} ion to $^5I_6$ and $^5F_4(^5S_2)$ level of Ho^{3+} ion respectively. After populating the excited states of the Ho^{3+} ion the Ho^{3+} ion makes various radiative and non-radiative transitions which leads to various emission peaks observed from the upconversion phosphor. The radiative transition from $^5F_4(^5S_2)$ to $^5I_8$ and $^5I_7$ levels of Ho^{3+} ion leads to the emission of 544 nm and 747 nm wavelength light respectively. During energy transfer process non-radiative transitions also occur which increase the sample temperature. This temperature rise in ethanol suspension is measured and is discussed in next section.

The variation of emission intensity with increase in excitation power tells us number of photons involved in the upconversion emission process. For this upconversion emission spectra were recorded at various excitation powers. For upconversion emission process the emission intensity varies with pump power according to the relation $I \propto P^n$,[7,8,27,28] where I is the upconversion emission intensity; P is the pump power and n is the number of photons involved in a particular emission. In Fig. 6(a) emission spectra are plotted for five different pump powers and from this data $\ln P$ *vs.* $\ln I$ graph was plotted and shown in Fig. 6(b). From the linear fit the slope '*n*' was measured for all three emission bands. In each case slope value is in the range of 1.65–1.94 which suggests that all emission bands occur due to the two-photon absorption process.

Decay time for $^5F_4(^5S_2) \rightarrow {}^5I_8$ and $^5F_5 \rightarrow {}^5I_8$ transitions of Ho^{3+} ion was measured using 980 nm excitation. The expression that relates the emission intensity and the decay time as[26]

$$I(t) = I_0 \exp\left(-\frac{t}{\tau}\right) \qquad \text{(v)}$$

where I_0 and $I(t)$ are the emission intensity at the initial time (at $t = 0$) and at time t,respectively. t is the time and τ is the decay time of emitting level. From the above equation, it can be seen that at decay time *i.e.*, at $t = \tau$, intensity becomes $1/e$ times the initial intensity *i.e.*, $I(t) = I_0/e$. Fig. 7 shows the decay curves for 544 nm and 650 nm emissions. It is observed that decay time of $^5F_4(^5S_2)$ level is slightly higher than the $^5F_5$ level. Decay times are mentioned in figure.

3.6. Photo-thermal conversion efficiency

The use of photothermal reagents in photo-thermal therapy is based on desired NIR absorption and good photothermal

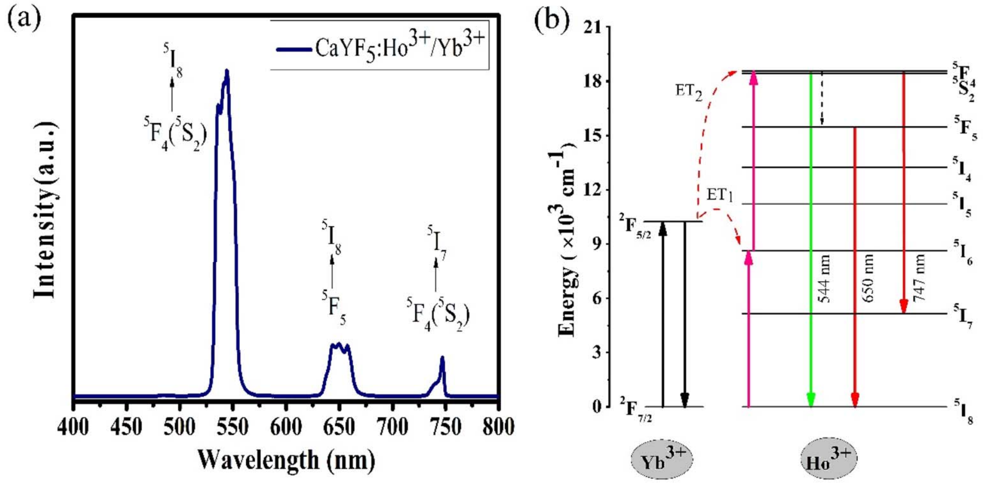

Fig. 5 (a) The upconversion emission spectrum for $CaYF_5$:Ho^{3+}/Yb^{3+} upconversion phosphor and (b) a possible energy level diagram.

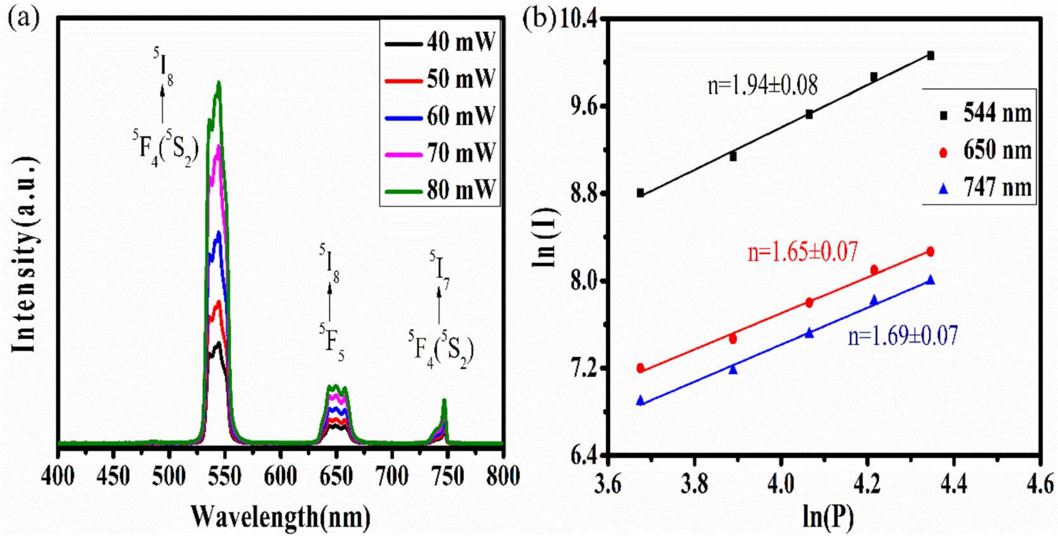

Fig. 6 (a) The power-dependent upconversion spectra and (b) the double logarithmic plot for calculation of the number of photons.

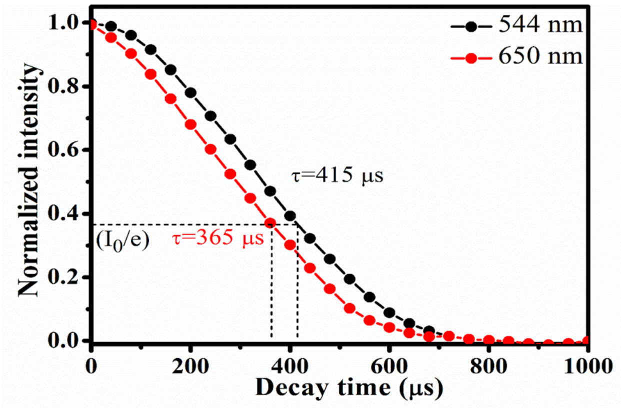

Fig. 7 Decay profile for 544 nm and 650 nm emission from $CaYF_5$:Ho^{3+}/Yb^{3+} upconversion phosphor upon 980 nm irradiation (indicated the 1/*e* times of initial intensity).

conversion efficiency. The photothermal conversion efficiency 'η' signifies the amount of heat converted from absorbed radiation. The expression that gives a relation between laser power, absorbance, and heat produced by the sample is given by[29]

$$\eta = \frac{C_p \dfrac{T_{\max} - T_\infty}{\tau_p} - Q_0}{P\left(1 - 10^{-A_\lambda}\right)} \quad \text{(vi)}$$

where C_p is the specific heat of upconversion phosphor dispersion, T_∞ and $T_{\max}$ are the surrounding temperature and maximum temperature attained on laser irradiation. P is laser power and τ_p is the time constant. A_λ is the absorbance of upconversion phosphor at the excitation wavelength. Q_0 is the heat dissipated by the cuvette and solvent. To determine Q_0, we recorded the temperature profile of the cuvette-containing suspension of 9 mg of upconversion phosphor and 2 ml of ethanol. The eqn (vi) could also be written as[29]

$$\eta = \frac{C_p \dfrac{T_{\max} - T_\infty}{\tau_p} - C_{p0} \dfrac{T_{\max,0} - T_{\infty,0}}{\tau_{p,0}}}{P\left(1 - 10^{-A_\lambda}\right)} \quad \text{(vii)}$$

where C_{p0} is the heat capacity of the cuvette solvent system without upconversion phosphor. $T_{\infty,0}$ and $T_{\max,0}$ are the surrounding temperature and maximum temperature attained by the cuvette solvent system upon laser irradiation. $\tau_{p,0}$ is the time constant for the temperature rise of the cuvette solvent system. The parameter-specific heat is related to the concentration of upconversion phosphor dispersion but here sufficiently low concentration (20 mM) of upconversion phosphor was used and hence as an approximation $C_p = C_{p0}$.

Now the eqn (vii) can be rewritten as

$$\eta = \frac{C_p}{P} \frac{\dfrac{T_{\max} - T_\infty}{\tau_p} - \dfrac{T_{\max,0} - T_{\infty,0}}{\tau_{p,0}}}{\left(1 - 10^{-A_\lambda}\right)} \quad \text{(viii)}$$

By using eqn (viii), photo-thermal conversion efficiency was calculated and it found to be 57.9%. This value is closer to other such reports.[30] The temperature rise with time upon laser irradiation is shown in Fig. 8(a). The parameters associated with the temperature profile were calculated and shown in Table 1. The synthesized $CaYF_5$:Ho^{3+}/Yb^{3+} upconversion phosphor also shows good stability in ethanol. The emission from the sample was recorded for 12 h and shown in Fig. 8(b). Very small change in emission intensity is observed after 12 h.

3.7. Temperature-dependent upconversion emission study

To study the competency of the upconversion phenomenon with temperature for the synthesized $CaYF_5$:Ho^{3+}/Yb^{3+} upconversion phosphor, temperature-dependent upconversion spectra were recorded. The competency assessment of upconversion emission with temperature is a requirement for upconversion phosphor being used for temperature-related

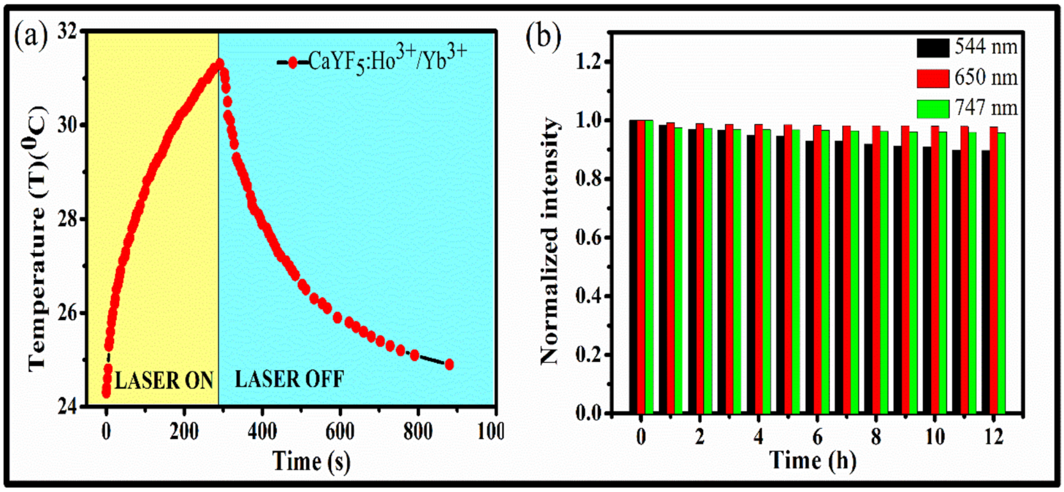

Fig. 8 (a) Temperature profile for radiation to heat conversion and (b) stability of upconversion phosphor dispersion upon 980 nm irradiation.

Table 1 Calculated parameter values associated with the temperature profile of upconversion phosphor dispersion and without upconversion phosphor dispersion

Sample	Parameter	Unit	Laser ON	Laser OFF	Average
$CaYF_5$:Ho^{3+}/Yb^{3+}	$T_{max} - T_{\infty}$	°C	7	140.2	129.9
	τ_p	s	119.7		
Ethanol	$T_{max,0} - T_{\infty,0}$	°C	2.1	105.2	119.1
	$\tau_{p,0}$	s	133.1		

applications like thermometry and photodynamic therapy. The dopant ions have various energy levels, some of which are thermally coupled and some are non-thermally coupled. The ways of populating these energy levels and decay pathways are strongly dependent on the temperature of the environment. For these systems, the variation in population density with temperature for any specific energy level is governed by the Boltzmann relation while the decay rate is governed by the Arrhenius equation. Generally, a decreasing trend of upconversion emission intensity has been observed with an increase in temperature and it is termed thermal quenching. Since all transitions are dependent on temperature but they are not equally dependent on temperature hence the ratio of the intensity of emission for two different wavelengths at each temperature value does not remain constant. This is true for both thermally coupled and non-thermally coupled level systems. One can use this intensity variation phenomenon to measure the sensitivity and hence its compatibility for thermometric applications. In the present case, the system is considered a non-thermally coupled system due to the lack of thermally coupled energy levels in the Ho^{3+} ion.

The temperature of the sample was increased using a small heater. As the voltage in the potentiometer increases the temperature of the heater and upconversion phosphor increases. The variation in emission intensity is shown in Fig. 9(a). The increase in temperature causes a decrease in emission intensity due to an increased rate of multi-phonon relaxation and hence non-radiative transitions and referred to as thermal quenching of upconversion emission.[31] This effect is deleterious to upconversion emission but this can also be considered an advantage for some upconversion host materials because of its utility for optical thermometry applications. In some upconversion host lattices, the change in emission intensity is also associated with the change in the intensity ratio of two emissions. This intensity ratio is referred to as fluorescence intensity ratio (FIR) and it is associated with the thermal response of that material. By exploiting this property those rare earth-doped host materials can be utilized as thermal sensors. Here in our case, we investigated the above-discussed property for the synthesized upconversion phosphor. Here we considered the ratio of 544 nm emission wavelength to 650 nm emission wavelength and the change in FIR is shown in Fig. 9(b). Here it can be seen that the data fit the exponential decay type function and the relation between FIR and temperature is shown in the graph.

By using this relation, the FIR and temperature were calculated the absolute and relative sensitivity for upconversion phosphor were calculated using following relations:

The expression for absolute sensitivity is

$$S_A = \left|\frac{d(\mathrm{FIR})}{dT}\right| \tag{ix}$$

And relative sensitivity is,

$$S_R = \left|\frac{1}{\mathrm{FIR}}\frac{d(\mathrm{FIR})}{dT}\right| \tag{x}$$

where T is the temperature.[32]

By using these relations the calculated values for absolute and relative sensitivities are found to 14.2×10^{-3} K^{-1} and 0.0057 K^{-1} at 300 K, respectively. The variation in absolute and relative sensitivity is depicted in Fig. 10.

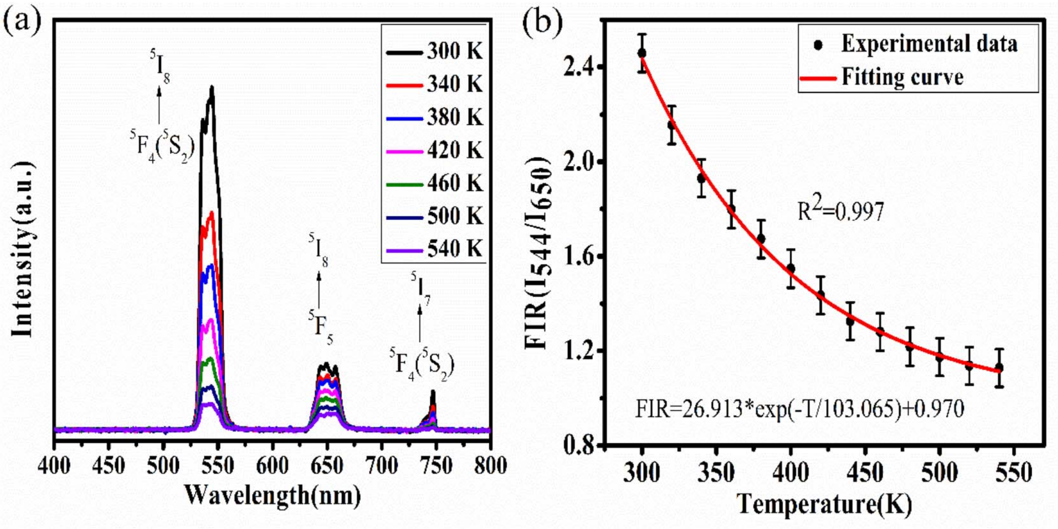

Fig. 9 Variation in (a) upconversion intensity and (b) FIR with temperature.

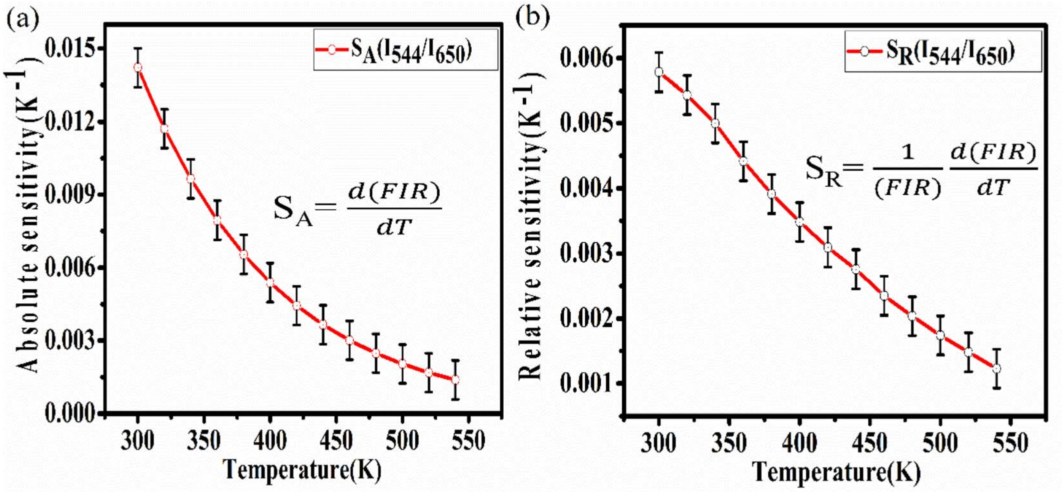

Fig. 10 Variation in (a) absolute sensitivity and (b) relative intensity with temperature.

4. Applications

4.1. Fingerprint detection and security ink

Fingerprint detection is the first and most important evidence which is crucial in any criminal investigation. It is very important to identify the involvement of any person in any crime hence the first step is to collect the fingerprint from the crime scene or objects at the crime scene like a weapon or other materials. The fingerprint can be anywhere like on the floor, books, furniture, glasses, or utensils. These surfaces can be porous, hard, metallic, magnetic, or non-magnetic. The current art of fingerprint detection is based on magnetism using commercially available iron oxide powder which provides good fingerprint detection and resolution but is not suitable for metallic or magnetic surfaces. Some more advanced application is the use of quantum dots and other luminescent material which can be excited using UV light but they also suffer from poor contrast hence the low quality of fingerprint.[33,34] Some upconversion nanoparticles have also been employed to detect fingerprints using a NIR laser source. Here we'll use the synthesized $CaYF_5:Ho^{3+}/Yb^{3+}$ upconversion phosphor for fingerprint detection on various surfaces.

Authors have selected glass slide, aluminium foil, debit card, compact disc (CD), ceramic tile, and wooden plate for the study. A volunteer had deposited fingerprints on these surfaces carefully. Then the upconversion phosphor powder was sprinkled on the surface and wiped out softly. Afterward, NIR illumination and scanning was performed using a 980 nm laser diode and a camera was used to record the image. The fingerprint obtained before and after illumination are shown in Fig. 11. In all surfaces finger patterns are clearly readable however, for Aluminium foil and debit card colour intensity is slight lower than the other cases.

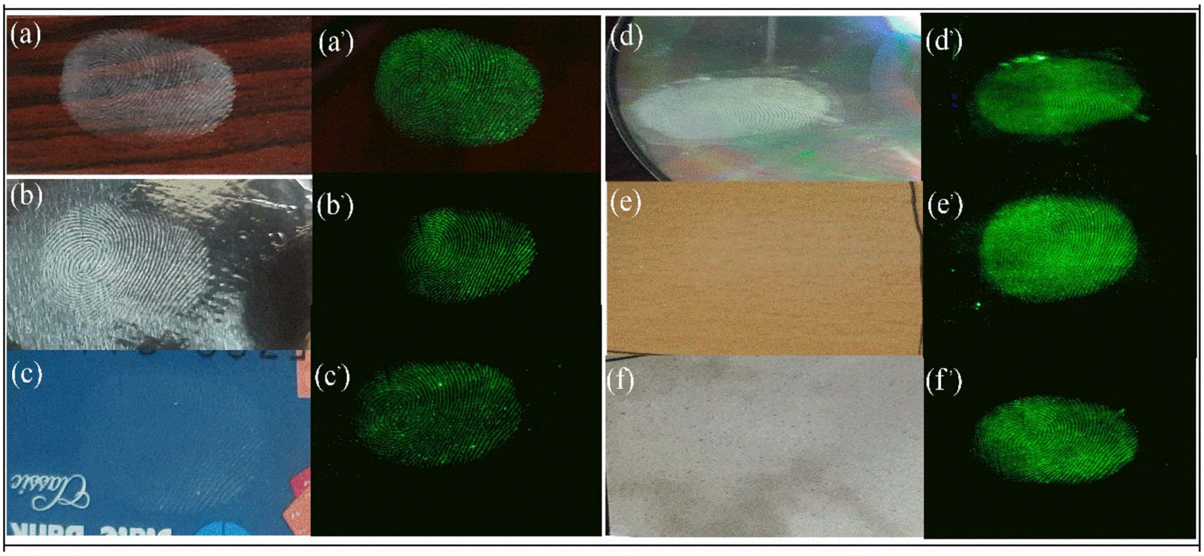

Fig. 11 Fingerprint detection using synthesized $CaYF_5:Ho^{3+}/Yb^{3+}$ upconversion phosphor on various surfaces before (left) and after 980 nm illumination (right) (a, a′) on a glass slide, (b, b′) on aluminum foil, (c, c′) on a debit card, (d, d′) on compact disk (CD), (e, e′) on a wooden block, (f, f′) on ceramic tile.

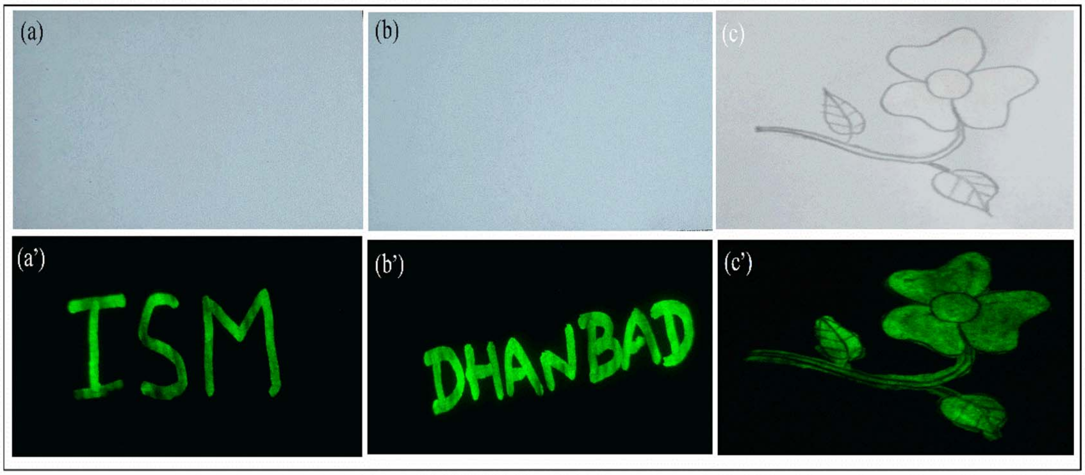

Fig. 12 Demonstration of security ink for anti-counterfeiting applications using synthesized $CaYF_5:Ho^{3+}/Yb^{3+}$ upconversion phosphor. (a), (b), and (c) is before NIR illumination while (a′), (b′), and (c′) is after NIR illumination.

The application of luminescent material as security ink is one of the major approaches that gained rapid attention for anti-counterfeiting agents. Here we demonstrated the application of $CaYF_5:Ho^{3+}/Yb^{3+}$ upconversion phosphor as security ink for anti-counterfeiting application. The invisible ink was prepared by dispersing the 25 mg of synthesized $CaYF_5:Ho^{3+}/Yb^{3+}$ upconversion phosphor into 4 ml of ethanol with a certain amount of polyvinylpyrrolidone (PVP 40) was added as stabilizer. The mixed solution was sonicated in an ultrasonic bath for 30 minutes to get a homogenous dispersion. Then few words like "ISM" and "DHANBAD" were written and a flower pattern was filled with this ink. Hidden words and flower is again clearly visible when a 980 nm laser beam was scanned over the area. Fig. 12 shows recorded words in green colour.

5. Conclusions

In summary, new $CaYF_5$ host was doped with Ho^{3+}/Yb^{3+} and upconversion emission and other studies were made. Elemental analysis using EDX experiment has confirmed the presence of all constituent elements. Absorption spectroscopies *viz.* UV-Vis-NIR and FTIR spectroscopy revealed the position of rare earth absorption bands and functional group present in the synthesized upconversion phosphor, respectively. Upconversion emission spectra were recorded and emission was observed at 544 nm, 650 nm, and 747 nm due to various transitions of Ho^{3+} ion. Pump power-dependent upconversion spectra provided insight into various energy transfer processes taking place while illumination with 980 nm wavelength. Decay time corresponding to $^5F_4(^5S_2)$ and $^5F_5$ levels were 415 μs and 365 μs, respectively. Photo-thermal conversion efficiency of prepared sample was found to 57.9% at 20 mM concentration of $CaYF_5$:Ho^{3+}/Yb^{3+} upconversion phosphor in ethanol. The high photothermal conversion efficiency is an indication that the synthesized upconversion phosphor can be a good photo-thermal agent in photo-thermal therapy. Temperature-dependent upconversion study suggests its suitability as optical thermometry. Moreover, successful demonstration of synthesized $CaYF_5$:Ho^{3+}/Yb^{3+} sample is done for latent fingerprint detection and security ink.

Conflicts of interest

There are no conflicts to declare.

Acknowledgements

Kumar Shwetabh is thankful to IIT (ISM) Dhanbad for providing financial support in terms of a senior research fellowship (SRF). K. Kumar acknowledges DST, New Delhi for financial support (SERB)/EMR/2017/000228.

References

1 R. Abdul Jalil and Y. Zhang, *Biomaterials*, 2008, **29**, 4122–4128.
2 A. Kavand, C. A. Serra, C. Blanck, M. Lenertz, N. Anton, T. F. Vandamme, Y. Mély, F. Przybilla and D. Chan-Seng, *ACS Appl. Nano Mater.*, 2021, **4**, 5319–5329.
3 D. Kumar, S. Verma, K. Verma, S. Som, V. Kumar and H. C. Swart, *Ceram. Int.*, 2018, **44**, 13649–13653.
4 T. Grzyb, S. Balabhadra, D. Przybylska and M. Węcławiak, *J. Alloys Compd.*, 2015, **649**, 606–616.
5 S. Som, C.-Y. Yang, C.-H. Lu and S. Das, *Ceram. Int.*, 2019, **45**, 5703–5709.
6 S. K. Singh, K. Kumar and S. B. Rai, *Sens. Actuators, A*, 2009, **149**, 16–20.
7 M. M. Upadhyay and K. Kumar, *J. Rare Earths*, 2022, DOI: 10.1016/j.jre.2022.07.005.
8 N. Kumar Mishra, M. M. Upadhyay, S. Kumar and K. Kumar, *Spectrochim. Acta, Part A*, 2022, **282**, 121664.
9 K. Shwetabh, S. K. Maurya, A. Banerjee, R. Poddar and K. Kumar, *New J. Chem.*, 2022, **46**, 21950–21961.
10 M. I. Sarkar, N. K. Mishra and K. Kumar, *Methods Appl. Fluoresc.*, 2022, **11**, 014002.
11 W. Gao, X. Kong, Q. Han, Y. Chen, J. Zhang, X. Zhao, X. Yan, J. Liu, J. Shi and J. Dong, *J. Lumin.*, 2018, **202**, 381–387.
12 W. Gao, J. Dong, Z. Wang, Z. Zhang and H. Zheng, *Mater. Res. Bull.*, 2017, **91**, 77–84.
13 W. Gao, H. Zheng, E. He, Y. Lu and F. Gao, *J. Lumin.*, 2014, **152**, 44–48.
14 B. Zhou, Y. Wang and D. Xia, *RSC Adv.*, 2015, **5**, 66807–66814.
15 M. Bouffard, T. Duvaut, J. P. Jouart, N. M. Khaidukov and M. F. Joubert, *J. Phys.: Condens. Matter*, 1999, **11**, 4775.
16 J. Shin, J.-H. Kyhm, A.-R. Hong, J. D. Song, K. Lee, H. Ko and H. S. Jang, *Chem. Mater.*, 2018, **30**, 8457–8464.
17 M. Xing, W. Cao, H. Zhong, Y. Zhang, X. Luo, Y. Fu, W. Feng, T. Pang and X. Yang, *J. Alloys Compd.*, 2011, **509**, 5725–5730.
18 S. K. Jakka, M. J. Soares, M. P. F. Graça, A. J. Neves, P. C. Nagajyothi and P. K, *Opt. Mater.*, 2022, **129**, 112442.
19 P. Du, L. Luo and J. S. Yu, *J. Alloys Compd.*, 2015, **632**, 73–77.
20 Z. Tian, H. Yu, Z. Han, Z. Guan, S. Xu, J. Sun, Y. Cao, Y. Wang, L. Cheng and B. Chen, *Ceram. Int.*, 2022, **48**, 27836–27848.
21 R. Luo, L. Chen, Q. Li, J. Zhou, L. Mei, Z. Ning, Y. Zhao, M. Liu, X. Lai, J. Bi, W. Yin and D. Gao, *Inorg. Chem.*, 2020, **59**, 17906–17915.
22 G. H. Dieke, *Spectra and energy levels of rare earth ions in crystals*, 1968, p. 1968.
23 R. Gopal, A. Kumar and J. Manam, *Mater. Chem. Phys.*, 2021, **272**, 124960.
24 M. Patel, A. Chavda, I. Mukhopadhyay, J. Kim and A. Ray, *Nanoscale*, 2016, **8**, 2293–2303.
25 V. H. Mudavakkat, V. V. Atuchin, V. N. Kruchinin, A. Kayani and C. V. Ramana, *Opt. Mater.*, 2012, **34**, 893–900.
26 S. Sinha, M. Kumar Mahata and K. Kumar, *New J. Chem.*, 2019, **43**, 5960–5971.
27 R. Krishnan, S. G. Menon, D. Poelman, R. E. Kroon and H. C. Swart, *Dalton Trans.*, 2021, **50**, 229–239.
28 J. F. Suyver, A. Aebischer, S. García-Revilla, P. Gerner and H. U. Güdel, *Phys. Rev. B: Condens. Matter Mater. Phys.*, 2005, **71**, 125123.
29 S. Balabhadra, M. L. Debasu, C. D. S. Brites, R. A. S. Ferreira and L. D. Carlos, *Opt. Mater.*, 2018, **83**, 1–6.
30 Y. Dai, D. Yang, D. Yu, C. Cao, Q. Wang, S. Xie, L. Shen, W. Feng and F. Li, *ACS Appl. Mater. Interfaces*, 2017, **9**, 26674–26683.
31 Y. Wang, B. Chen and F. Wang, *Nanoscale*, 2021, **13**, 3454–3462.
32 Z. Li, L. Lin, Z. Feng, L. Huang, Z. Wang and Z. Zheng, *J. Lumin.*, 2021, **232**, 117873.
33 J. Liu, Z. Shi, Y. Yu, R. Yang and S. Zuo, *J. Colloid Interface Sci.*, 2010, **342**, 278–282.
34 A. Xu, G. Wang, Y. Li, H. Dong, S. Yang, P. He and G. Ding, *Small*, 2020, **16**, 2004621.